

# Rock Salt Oxide Hollow Spheres Achieving Durable Performance in Bifunctional Oxygen Energy Cells

Po-Chun Liao, Ren-Huai Jhang, Yu-Hsiang Chiu, Joey Andrew A. Valinton, Chia-Hao Yeh, Virgilio D. Ebajo, Jr., Ching-Hsuan Wang, and Chun-Hu Chen\*



Cite This: *ACS Appl. Energy Mater.* 2021, 4, 3448–3459



Read Online

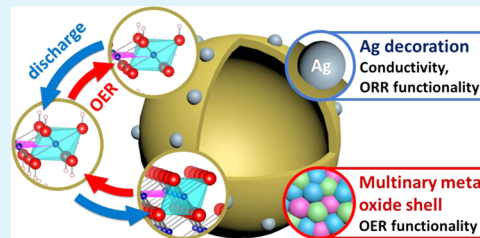
ACCESS |

Metrics & More

Article Recommendations

Supporting Information

**ABSTRACT:** The interchangeable operation of alkaline oxygen evolution and reduction using bifunctional electrocatalysts in devices consolidates the commercialization milestone of energy storage in hydrogen, and yet, it is usually limited by issues of carbon corrosion in electrocatalysts and inhomogeneous electrode fabrication. Here, we demonstrate a synthetic route toward carbon-free ternary rock salt oxide (i.e., NiO/CoO/FeO) hollow spheres with silver decoration on the surface for durable operation in bifunctional cells. These Ag-decorated ternary oxides exhibit an overall bifunctional potential gap ( $\Delta E = E_{j10,\text{OER}} - E_{j\text{half},\text{ORR}}$ ) of 0.89 V. Operando Raman studies show that the rock salt structure shows the phenomenon of a highly reversible local environment during the charge–discharge OER cycles, a key characteristic for high durability in bifunctional devices. At equivalent content between Ni and Co, NiOOH is the main OER-active species with CoOOH and/or CoO<sub>2</sub> as the cocatalyst, where the presence of the FeO dopant facilitates structural activation and reversibility. With the proof-of-concept performance in anion-exchange membrane (AEM) devices, the catalysts achieve a durable cyclic operation with a high current density (1000 mA cm<sup>-2</sup>) at smaller potentials (2.03 V) than RuO<sub>2</sub> (2.16 V) under the electrolyzer mode, while it can yield two times greater power density (96.98 mW cm<sup>-2</sup>) than Pt/C (53.58 mW cm<sup>-2</sup>) in the fuel cell mode.



**KEYWORDS:** rock salt, bifunctional cell, carbon free, oxygen evolution, oxygen reduction, operando Raman

## 1. INTRODUCTION

Finding scale- and cost-effective storage for intermittent green energy poses a critical challenge for the future commercialization of the sustainable energy industry.<sup>1,2</sup> Highly efficient electrocatalysts active for both oxygen evolution reaction (OER) and oxygen reduction reaction (ORR) in a single cell ideally overcome the challenge of minimizing device dimensions and fabrication costs in massive-scale power stacks.<sup>3–5</sup> However, the interchangeable operation between oxidative OER and reductive ORR significantly decays carbon-based electrocatalysts, such as commercial benchmark Pt/C, where the low-density nature of carbon dots enables excellent dispersion for uniform electrode fabrication.

Mimicking Pt/C by using different dimension carbon supports, such as graphene, leads to severe aggregation due to the 2D nature of the sheet structure.<sup>6–8</sup> Because carbon corrodes rapidly under highly oxidative OER and disintegrates due to thermodynamic instability under ORR,<sup>9</sup> a carbon-free strategy represents a rational design of durable electrocatalysts for bifunctional devices.<sup>3,10</sup> Metal oxide materials are promising replacements for carbon due to their high stability under alkaline OER conditions, but they are generally too dense to maintain dispersion homogeneity.

Doping impurities in metal oxides is an effective approach to improve conductivity and activities. As such, homogeneous mixing of multiple metals in a single oxide phase enables a

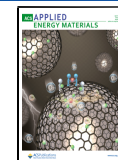
drastic reduction of the intrinsic electrical resistivity.<sup>10,11</sup> However, studies show that Co–Ni binary oxides, as highly OER-active species, tend to form separate phases (e.g., NiO and Co<sub>3</sub>O<sub>4</sub>) at varying Co/Ni ratios.<sup>12</sup> We proposed to utilize rock salt oxide as the common structure to incorporate Co and Ni into a single phase with an identical local environment.<sup>13,14</sup> Enhanced intrinsic conductivity and structure stability in cyclic, bifunctional electrocatalysis are anticipated. Although rock salt oxides of Ni and Co solid solution have been known for more than half a century,<sup>15</sup> their bifunctional purpose has not been well recognized.

Our rational approach involves constructing OER-active rock salt oxide spheres with hollow structures, aiming to lower the density and enhance dispersion homogeneity (see Scheme 1). Analogous to Pt/C, we substitute more affordable Ag instead of Pt on the sphere surface to achieve ORR activity. Studies show that the heterojunction between silver and metal oxides can balance adsorption and desorption kinetics of oxygen, an essential property to achieve comparable ORR

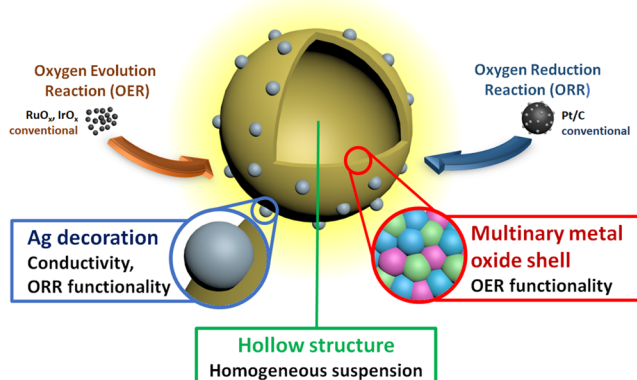
**Received:** December 24, 2020

**Accepted:** March 10, 2021

**Published:** March 22, 2021



**Scheme 1. Design Concept of a Carbon-Free Bifunctional Electrocatalyst<sup>a</sup>**



<sup>a</sup>The multinary rock salt oxide shell (NiO, CoO, and FeO) is responsible for the oxygen electrochemical evolution functionality (before the OER activation), instead of using Ru- and Ir-based oxides. Ag decoration on the shell aims to mimic the role of Pt in Pt/C for the ORR functionality. The hollow structure affords a lowered density to achieve a reasonable dispersion capability.

kinetics to Pt.<sup>16,17</sup> Moreover, to further improve OER activity, the as-prepared NiO–CoO rock salt oxides serve as a structure-directing matrix to stabilize an Fe dopant as rock salt FeO, rather than another thermodynamically favored phase (e.g., hematite). To understand the local structural dynamics of the as-yielded ternary rock salt oxides, operando Raman spectroscopy reveals a highly reversible local coordination under charge–discharge OER cycles, a desired characteristic to

aid durable device operation. The anion-exchange membrane (AEM) cells perform repetitive fuel cell–electrolyzer interchange functionality without significant decay in current density and electrochemical impedance. In addition, the rock salt hollow sphere composites exhibit superior electrolyzer and fuel cell performance to benchmarks (RuO<sub>2</sub> and Pt/C). The combined strategy of a carbon-free hollow sphere and ternary rock salt oxide is highly effective to achieve a bifunctional cell operation with great durability.

## 2. RESULTS AND DISCUSSION

**2.1. Synthesis of Silver-Decorated NiO–CoO Hollow Spheres.** The NiO–CoO hollow spheres (NCO-HSs) were first prepared by a two-step procedure (see the Supporting Information for details).<sup>8,16</sup> The SEM images (Figure 1a) reveal that the NCO-HS exhibits uniform spheres with diameters of 150–200 nm and a smooth surface.<sup>18</sup> The TEM images (Figure 1b) confirm the presence of a hollow core in NCO-HS with a shell thickness of 30–45 nm, as well as the absence of other impure structures. To decorate Ag nanoparticles on the surface of NCO-HS, we utilized (3-aminopropyl)trimethoxysilane (APTMS) to functionalize the surface with terminal amine groups for coordination with Ag<sup>+</sup>, which was further reduced by refluxing in DMF.<sup>19</sup> The entire synthesis is summarized in Figure S1a. As shown in Figure 1c,d, Ag nanoparticles ( $17.28 \pm 7.69$  nm, Figure S1b) were seen to be attached on the surface, while the hollow-core structures remained intact. The EDS elemental mapping (Figure 1g) confirms the homogeneous distribution of Ni (green) and Co (red) in the shell, while the Ag signals (blue) are shown on particles decorated around the Ni/Co oxide shell. This agrees with the high-resolution (HR) TEM images

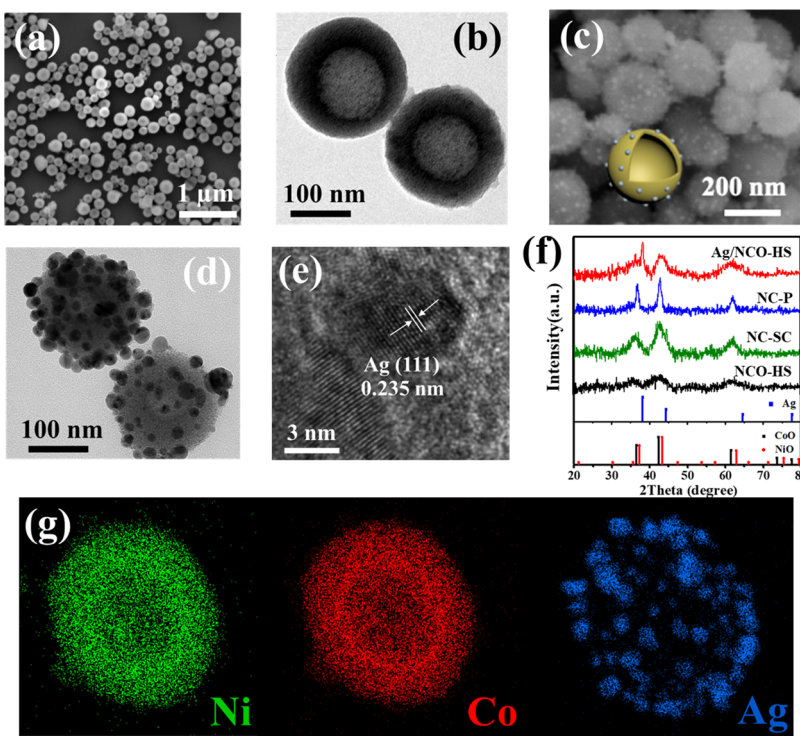


**Figure 1.** Characterization of the prepared rock salt oxide spheres. (a) SEM and (b) TEM images of NiO–CoO hollow spheres (NCO-HS). (c) SEM and (d) TEM images of Ag-decorated NCO-HS (Ag/NCO-HS). (e) HR-TEM image of Ag/NCO-HS showing the lattice fringes pertaining to Ag. (f) XRD patterns of Ag/NCO-HS, NCO-P, powdered NCO (NCO-P), and solid-core NCO (NCO-SC). (g) EDS mapping of Ni, Co, and Ag of an individual Ag/NCO-HS.

(Figure 1e), indicating that the decorated particles contain a lattice fringe of 0.235 nm corresponding to Ag(111). The atomic ratios of Co to Ni are nearly one and in agreement with the equivalent amounts of the precursors in the reaction mixture (Figures 1g and S2).

Although the XRD patterns of NCO-HS correspond to rock salt NiO and CoO (Figure 1f), the significant peak broadening results in the difficulty of exclusive phase identification.<sup>19</sup> The small deviations among their characteristic peaks are due to the differences in their unit cell parameters caused by the unequal ionic radii (i.e., Ni<sup>2+</sup> and Co<sup>2+</sup> have ionic radii of 0.72 and 0.69 Å, respectively).<sup>20</sup> Thus, we further studied the crystallinity evolution of NCO-HS at various temperatures in air (Figure 2). No observable change in the pattern occurred at lower

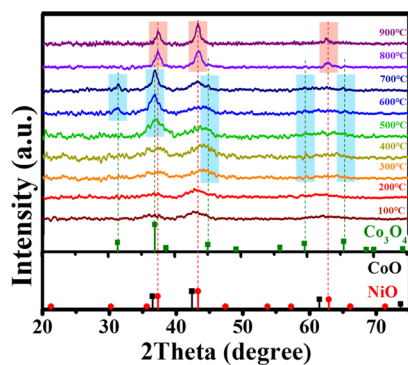


**Figure 2.** Phase transformation of NCO-HS monitored by XRD at a calcination temperature range from 100 to 900 °C. The Co<sub>3</sub>O<sub>4</sub> phase occurs from 300 °C and then disappears at 800 °C (see the blue bar labels). The co-existing NiO and Co<sub>3</sub>O<sub>4</sub> phases change into a single phase as the temperature reaches 800 °C, corresponding to a rock salt CoO–NiO solid solution of NCO-HS.

temperatures until at 300 °C, where additional peaks at  $2\theta$  of 59.46 and 65.13° appeared prominently due to increased crystallinity. At 500–700 °C, the diffraction peaks emerge at 31.31, 36.92, 44.85, 59.46, and 65.13° corresponding to the crystal indices of Co<sub>3</sub>O<sub>4</sub> at (220), (311), (400), (511), and (440), respectively. At 700–800 °C, the Co<sub>3</sub>O<sub>4</sub> phase starts to

transform into the fcc CoO phase and eventually becomes the fcc NiO phase at 900 °C. In retrospect, this observed temperature-dependent crystal phase evolution is highly consistent with the earlier report on rock salt NiO–CoO,<sup>13</sup> further confirming that the synthesis of NCO-HS is a rare example of directly producing a nanocrystalline NiO–CoO solid solution at low temperatures (<200 °C), compared to those at 800 °C.<sup>13</sup>

The elemental compositions of NCO-HS and Ag/NCO-HS were investigated by X-ray photoelectron spectroscopy (XPS) (Figure S3). In NCO-HS, the divalent state of Ni<sup>II</sup> and Co<sup>II</sup> is confirmed based on the observed binding energies of Ni [Ni 2p<sub>3/2</sub> at 854.3 eV (satellite peak at 860.0 eV) and 2p<sub>1/2</sub> at 872.3 eV (satellite peak at 878.4 eV)]<sup>21</sup> and of Co [Co 2p<sub>3/2</sub> at 779.6 eV (satellite peak at 784.8 eV) and 2p<sub>1/2</sub> at 795.4 eV (satellite peak at 801.6 eV)], with a peak difference of 15.8 eV (Figure S3b),<sup>22</sup> respectively. These agree with the rock salt NiO–CoO phase in the XRD data. In the case of Ag/NCO-HS, the binding energy of NiO and CoO increases by 1.2 and 1.4 eV, respectively, as compared to NCO-HS, while XPS signals of silver at 367.8 eV (3d<sub>5/2</sub>) and 374.0 eV (3d<sub>3/2</sub>) are lower by 0.4 eV than typical values reported in the literature (Figure S3c).<sup>23</sup> These observations are the result of the inhomogeneous distribution of electron density associated with the presence of a metal/metal oxide heterojunction site. The binding energy shifts suggest the polarization of the interactions between Ni<sup>2+</sup>/Co<sup>2+</sup> and Ag. The increased cationic character in Ni<sup>2+</sup> and Co<sup>2+</sup>, based on theoretical XPS studies,<sup>24</sup> facilitates their conversion into higher valence states as active OER species by Ag decoration.<sup>25</sup> In an earlier study on Ag@Co(OH)<sub>2</sub>, observed higher XPS shifts in Co<sup>2+</sup> affected by Ag decoration became correlated with the electron deficiency of the former, according to theoretical models.<sup>26</sup> Consequently, Ag becomes an electron acceptor, which also promotes electron transfer in ORR.<sup>27</sup> Such compartmentalization of species with a lowered binding energy as ORR active or otherwise as OER active has been displayed on various metal–metal oxide heterojunction materials.<sup>27–30</sup> In this manner, the heterojunction created by the Ag addition can result in the enhancement of the reactions catalyzed by each component.

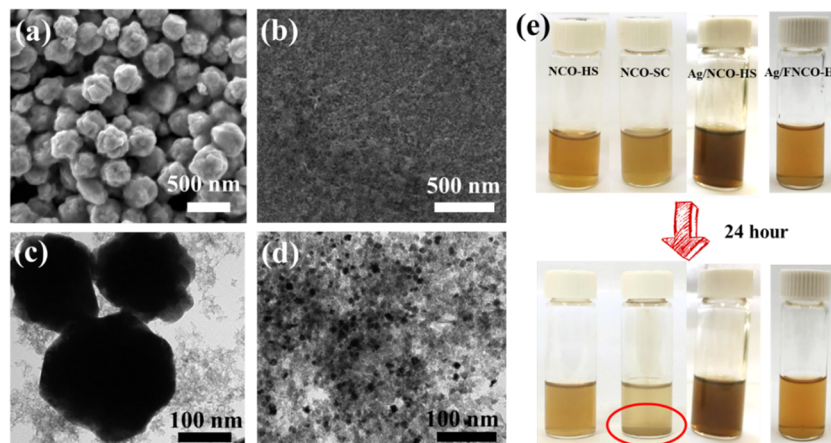


**Figure 3.** Characterization of control samples and suspension tests. (a) SEM and (c) TEM images of the samples prepared using the oleylamine-free procedure yielding solid-core samples (NCO-SC). (b) SEM and (d) TEM images of the samples prepared using a TBAOH-free procedure showing nanoflakes instead of a spherical morphology. (e) Suspension tests of NCO-HS, NCO-SC, Ag/NCO-HS, and Ag/FNCO-HS in a water/IPA solution. After 24-h aging, all of the hollow structure samples remain well suspended, except for NCO-SC (precipitates are indicated by the red circle).

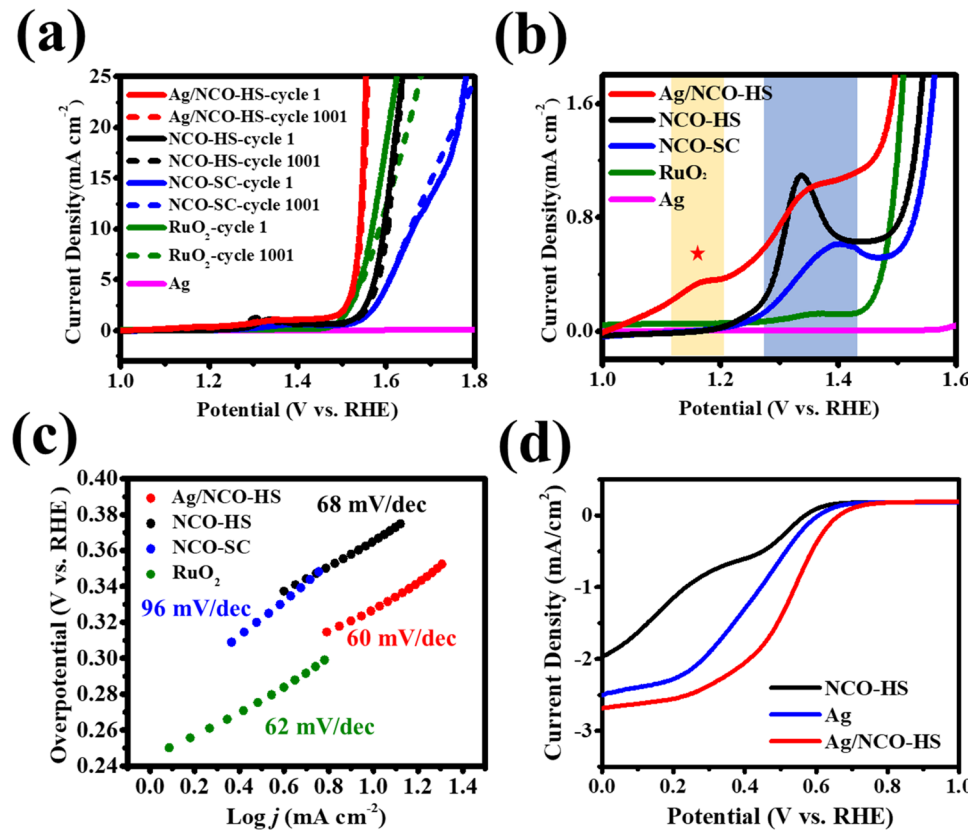


**Figure 4.** Electrocatalytic performance comparison. (a) OER LSV curves of the samples in 0.1 M KOH at a rotation of 1600 rpm. (b) The magnified OER LSV curves of (a) reveal the potentials for oxidation number changes of Ni and Co in the electrocatalysts. Two peak regions labeled by yellow and blue correspond to Co and Ni oxidation signals, respectively. (c) OER Tafel plots of the electrocatalysts. (d) ORR LSV curves of the samples recorded at 1600 rpm in O<sub>2</sub>-saturated 0.1 M KOH (counter electrode: glassy carbon).

To understand the roles of oleylamine and TBAOH in hollow structure formation, control experiments of oleylamine- and TBAOH-free syntheses were carried out. In the absence of oleylamine, spherical shapes with solid-core characteristics (denoted NCO-SC) form, according to the SEM and TEM images (Figure 3a,c), indicating that oleylamine may serve as a soft template for hollow structure formation.<sup>31</sup> Meanwhile, synthesis in the absence of TBAOH results in irregular, fine particles (<15 nm Figure 3b,d). By suspending equal masses of either hollow-core or solid-core samples in water (Figure 3e), the suspensions of the former (NCO-HS and Ag/NCO-HS) remain dispersed over 24 h, while those of the latter result in sedimentation of particles. Thus, the low-density hollow structure to acquire high dispersion ability is well justified.

**2.2. Electrocatalytic Oxygen Evolution.** The OER performance of the prepared catalysts was evaluated by linear sweep voltammetry (LSV) under O<sub>2</sub>-saturated 0.1 M KOH (Figure 4a,b). NCO-HS exhibits a lower onset potential at 1.45 V than NCO-SC (1.49 V) and a smaller overpotential ( $\eta$  at 10 mA cm<sup>-2</sup>) of 360 mV than 422 mV of NCO-SC. The hollow structure of NCO-HS possibly enables efficient mass transport,<sup>32,33</sup> resulting in greater OER activity than the solid-core samples.

As compared to NCO-HS, Ag/NCO-HS exhibits a more superior OER activity with a lower onset potential (1.40 V) and overpotential (310 mV). No obvious OER activity is observed in the LSV of pure Ag nanoparticles, revealing that the NiO–CoO surface mainly acts as the OER-active sites. In comparison, Ag/NCO-HS shows higher performance than

commercial OER benchmark RuO<sub>2</sub> (onset potential of 1.42 V and  $\eta$  of 340 mV) and a high OER stability with negligible decay after 1000 sweeping cycles (Figure S4). Long-term durability tests of Ag/NCO-HS at a constant potential (1.63 V) exhibit 98% retention of its original current after 24 h, while RuO<sub>2</sub> retains only 23%, showing massive decay (Figure S5). After the durability test, SEM images of Ag/NCO-HS show insignificant morphological change and hollow structure retention (Figure S6). The corresponding ICP-MS analyses of the electrolyte solution postexperiment reveal a small amount of element leaching from Ag/NCO-HS (i.e., less than 0.5 mol %; see Figure S6), suggesting promising retention of structural integrity as compared to 20–30% leaching of the reported CoO<sub>x</sub> and CoFeO<sub>x</sub> within 6 h.<sup>34</sup> Elevated OER potentials generally lead to a higher probability of occurrence of structure distortion/defects. Due to this, the much faster cycles of bond breaking and re-formation can cause an irreversible alteration in coordination structures. Oxygen bubbling is also a strong force to detach Ag from the hollow sphere surface. The selected OER potential ranges enable a high catalytic conversion and bubble formation without exerting excessive electrocatalytic stress that can compromise the hollow structure as well as the attachment of Ag.

The presence of high oxidation states of the metal cations is essential to promote OER performance. The oxidation of Co<sup>II</sup> → Co<sup>III</sup> and Ni<sup>II</sup> → Ni<sup>III</sup> in the corresponding monometal oxide occurs around 1.15 and 1.45 V, respectively.<sup>14,35</sup> The shift of the Ni<sup>2+</sup>/<sup>3+</sup> transition (in voltage) toward the lower potentials (i.e., 1.33–1.35 V in Figure 4b) is associated with

the coexistence of Co and Ni ratios in the rock salt oxides. The stronger intensity of  $\text{Ni}^{2+}/\text{Ni}^{3+}$  peak in the hollow structure samples (NCO-HS) than the solid-core ones (NCO-SC) suggests more coverage of accessible  $\text{Ni}^{3+}$  sites because the thin shell of hollow spheres allows more facile activation than the impermeable cores (also see the ECSA study below).<sup>36</sup>

After Ag decoration, the LSV of Ag/NCO-HS (Figure 4b) shows two separate oxidation signals at 1.15 V (yellow band) and 1.35 V (blue band). The first peak (red star-labeled) corresponds to the  $\text{Co}^{2+}/\text{Co}^{3+}$  transition,<sup>14,37</sup> which means that Ag decoration stimulates Co activation compared to the Ag-free samples. The intense overlapping transitions between these two signals may suggest a sequential interaction starting from Co activation toward the Ni oxidation, contrary to an earlier report on the Co-inhibited transition of  $\text{NiO}$  to oxyhydroxide in the absence of Ag.<sup>14</sup> Despite the poor catalytic activity of stand-alone Ag particles, the OER enhancement delivered by Ag decoration on the rock salt oxides is consistent with the altered electronic structure at the heterojunction sites according to the above XPS data. This also implies a new activation pathway of this rock salt oxide-based composite.

In terms of OER kinetics, Tafel plots (Figure 4c) show that NCO-HS (68 mV dec<sup>-1</sup>) has superior kinetics compared to NCO-SC (96 mV dec<sup>-1</sup>) due to the performance associated with hollow structures.<sup>38</sup> Meanwhile, Ag/NCO-HS gives the lowest Tafel slope (60 mV dec<sup>-1</sup>), comparable to benchmark  $\text{RuO}_2$  (62 mV dec<sup>-1</sup>), showing that the Ag-decorated solid solution can reach OER kinetics similar to the benchmark. The electrochemical surface area (ECSA) comparison of these samples is shown in Figure S7. The ECSA of the hollow sphere samples, Ag/NCO-HS (23.7) and NCO-HS (20.6), is higher than that of NCO-SC (12.5) by 90 and 65%, respectively. The interior shell of the hollow structure provides more electrocatalytic active sites<sup>32</sup> than the solid-core samples, consistent with the OER activity trend (Figure 4a), where the presence of a hollow structure shows an increase in OER electrocatalytic performance.

In terms of mass activity (at  $\eta = 350$  mV), Ag/NCO-HS ( $489 \text{ A g}^{-1}$ ) is 3.85 times higher than benchmark  $\text{RuO}_2$  (Table S1). Meanwhile, its turnover frequency (TOF) ( $0.109 \text{ s}^{-1}$ ) is higher than that of  $\text{RuO}_2$  ( $0.0347 \text{ s}^{-1}$ ). Due to the Ag decoration, it has a higher mass activity (8.15 times higher) and TOF (9.4 times higher) than the silver-free sample (NCO-HS).

**2.3. Electrocatalytic Oxygen Reduction Reaction.** The ORR performance of NCO-HS shows its onset potential at 0.68 V, with two-step LSV curves corresponding to two-electron reduction (Figure 4d), commonly observed in transition-metal oxide electrocatalysts.<sup>8,16,39</sup> A two-step ORR usually leads to the release of hydrogen peroxide ( $\text{HO}_2^-$ ), which is highly corrosive to catalysts and the fuel cell membrane. Thus, a single-step ORR with a four-electron transfer is preferred. In comparison, Ag/NCO-HS shows a more positive onset potential (0.83 V) than NCO-HS and a one-step LSV curve with higher current density. The LSV change from a two-step to a one-step curve indicates that the silver decoration enables a four-electron reduction. Also, the presence of plateau currents of Ag/NCO-HS at around 0.3 V reveals a similar equilibrated oxygen adsorption and  $\text{OH}^-$  desorption kinetics to ORR by benchmark Pt/C. Compared to pure Ag nanoparticles in Figure 4d, the onset potentials of Ag/NCO-HS become slightly more positive, suggesting that the

Ag, influenced by the rock salt oxide through the heterojunction interface, mainly contributes to the ORR activity.<sup>16</sup>

The electron-transfer number values ( $n$ ) are presented in Figure S8. Ag/NCO-HS exhibits the greatest and most complete  $n$  value of 3.9 stretched over a wide potential range of 0.20–0.65 V, while NCO-HS only shows an incomplete reduction, with an  $n$  value close to 2 at around 0.6 V. The corresponding  $\text{HO}_2^-$  yields of NCO-HS and Ag/NCO-HS are 20 and 5% at 0.5 V, respectively (Figure S9), confirming that decorating Ag influences a complete, four-electron route and the inhibition of  $\text{HO}_2^-$ .<sup>40</sup> Electrochemical impedance spectroscopy (EIS) has shown that Ag decoration decreases the charge-transfer resistance to allow improved kinetics and electrocatalytic performance (Figure S10).<sup>16</sup> Methanol crossover,<sup>41</sup> which can potentially poison ORR catalysts in direct methanol fuel cells, can be tolerated by Ag/NCO-HS (see the details in Figure S11).

**2.4. Fe-Doped Oxides.** To further improve the OER activities of Ag/NCO-HS, a small amount of iron was introduced.<sup>42,43</sup> The iron oxide-doped  $\text{NiO}-\text{CoO}$  hollow spheres (denoted FNCO-HSs) were synthesized by adding the iron precursor in the first step of reflux (before the base addition), followed by the Ag decoration to yield Ag/FNCO-HS. The TEM images (Figure 5a) show similar morphologies

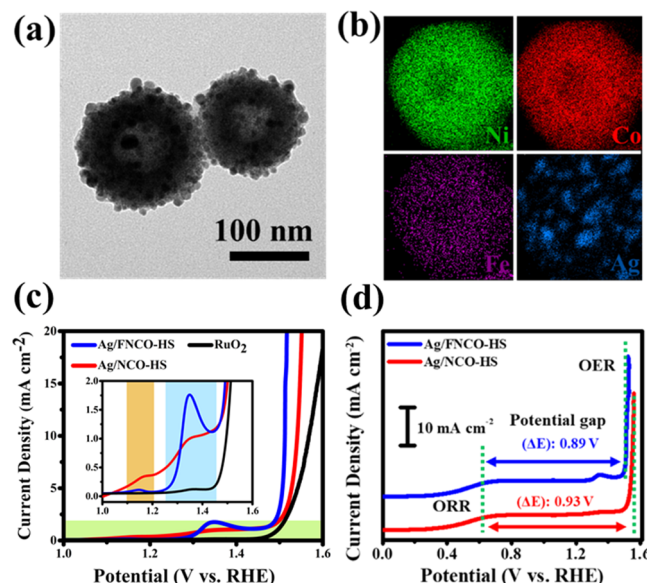


**Figure 5.** Characterization of Ag-decorated Fe-doped  $\text{NiO}-\text{CoO}$  hollow spheres (Ag/FNCO-HS). (a) TEM images of Ag/FNCO-HS. (b) EDS mapping of Ni, Co, Fe, and Ag of an individual hollow sphere. (c) OER LSV curves catalyzed by Ag/FNCO-HS in comparison with iron-free Ag/NCO-HS; the inset, which magnifies the green region, shows the peaks corresponding to  $\text{Co}^{2+}$  (orange band) and  $\text{Ni}^{2+}$  (light blue band) oxidation. (d) ORR and OER bifunctional activities of Ag/FNCO-HS with a potential gap smaller than Ag/NCO-HS by 40 mV.

to the binary Ag/NCO-HS with a uniform Ag particle distribution. The XRD patterns (Figure S12) also show a nearly identical phase to Ag/NCO-HS, suggesting no significant alterations in the rock salt structure due to iron oxide doping. In fact, reports show that Ni and Co oxide solid solutions stabilize the homogeneously introduced Fe.<sup>35,43</sup> The EDS mapping (Figure 5b) shows that all three metals are

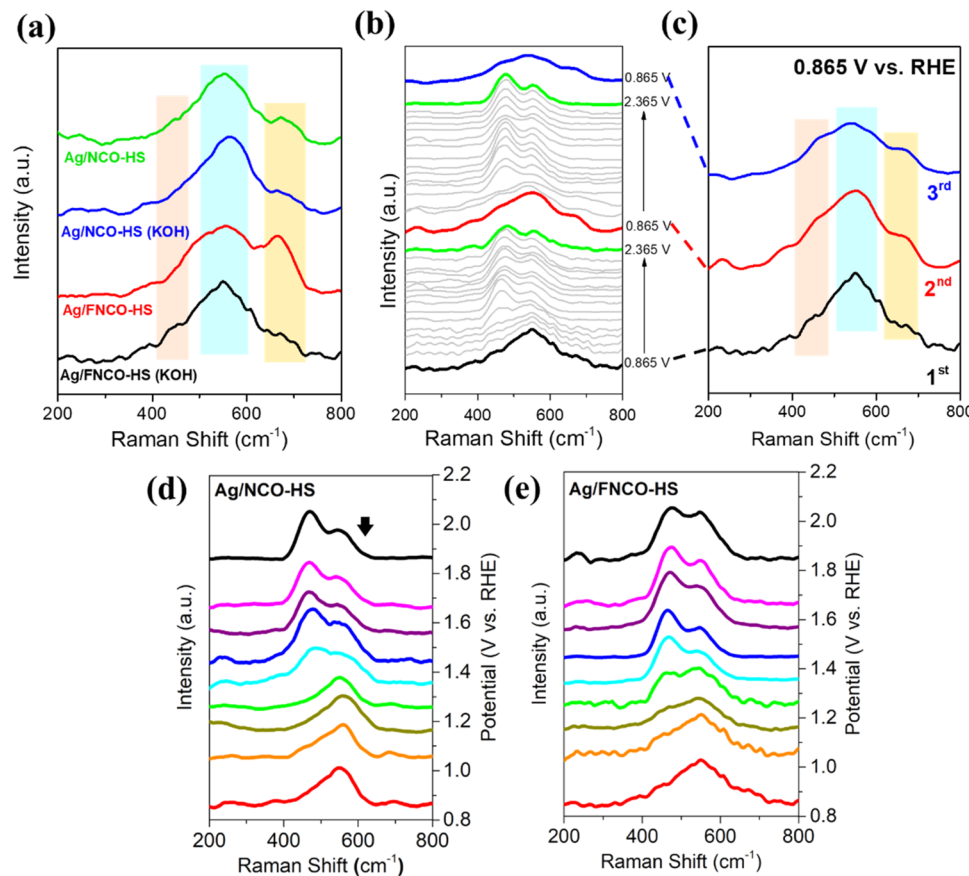


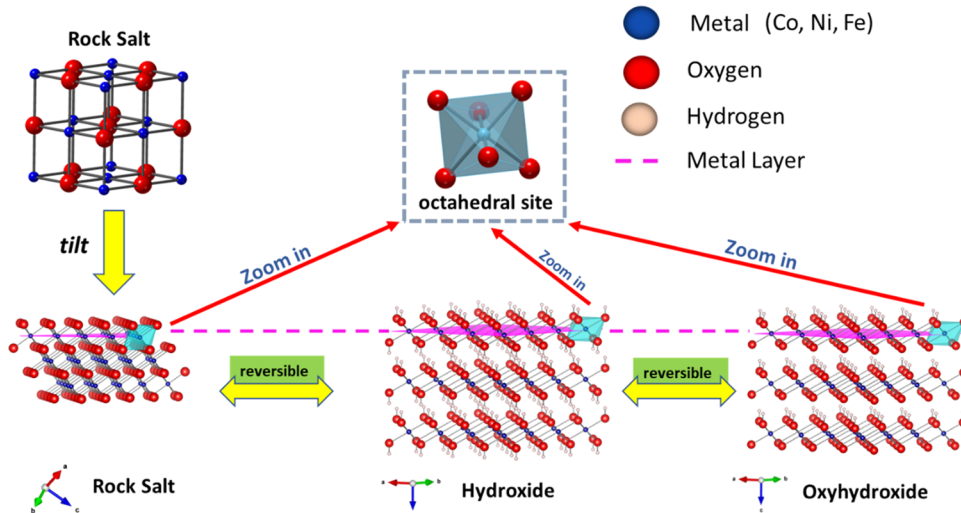
**Figure 6.** Raman studies of the electrocatalysts. (a) Comparison of Ag/NCO-HS and Ag/FNCO-HS in dry and KOH-immersed conditions. (b) Raman spectra of Ag/FNCO-HS associated with the charge–discharge OER cycles: charging from 0.865 to 2.365 V (black to green) and then return to the rest conditions at 0.865 V immediately (green to red). (c) Comparison of zero charge (0.865 V) curves acquired from (b) connected with the dashed lines. The notation of 1st, 2nd, and 3rd represents the rest conditions between two successive charge–discharge cycles. The pink, blue, and yellow highlights in (a) and (c) emphasize the Raman shift bands of 450, 550, and 670, cm<sup>-1</sup>, respectively. Operando Raman-coupled electrocatalysis of (d) Ag/NCO-HS and (e) Ag/FNCO-HS during the OER process; the arrow in (d) indicates the shoulder for the Co<sup>III</sup>OOH vibration. The right axes show the potential at which each Raman spectrum was measured.

evenly dispersed in the hollow spheres, while Ag is decorated on the outer surface. The ICP-MS (Table S2) shows 9% Fe doping in Ag/FNCO-HS. With the hollow-core structure, Ag/FNCO-HS retains suspension homogeneity, similar to Ag/NCO-HS, for at least 24 h (Figure 3e).

In comparison with the nondoped variant, the iron-doped samples show improved OER activities (i.e., 10% decrease in overpotential, Figure 5c), while the ORR onset potential shows no significant change (Figure S13) under identical Ag contents (Table S2). In the magnified LSV curve (inset of Figure 5c), the intensity of the Ni<sup>2+/3+</sup> transition peak at 1.35 V in Ag/FNCO-HS is much higher than that of the iron-free counterpart. This enhancement of Ni activation is similarly observed on Fe<sup>2+</sup>-added Ni<sup>2+/Fe<sup>3+</sup></sup>-layered double hydroxides<sup>44</sup> but contrary to the case of incorporating Fe<sup>3+</sup> in NiOOH.<sup>43</sup> Although the incorporated surface Fe<sup>3+</sup> on nickel (or cobalt) oxyhydroxides was recognized as a key active site for OER,<sup>42,43</sup> we hypothesize that Fe<sup>2+</sup> somehow retains its oxidation state and aids in activating Ni<sup>2+</sup>. Sun et al. found that the lowered overpotential of promoting Ni<sup>2+</sup> to higher valence states, which can be extended to a larger activated population, is due to the interaction of neighboring Fe<sup>2+</sup> with adjacent Ni<sup>2+</sup>,<sup>44</sup> but the amount of Fe<sup>2+</sup> must be kept at a minimum, which is highly consistent with the Fe-doped sample in this study. The overall bifunctional performance of a catalyst for

ORR and OER can be evaluated by the potential gap between ORR half-wave potentials and OER overpotentials at a current density of 10 mA cm<sup>-2</sup> ( $\Delta E = E_{j10, \text{OER}} - E_{j\text{half}, \text{ORR}}$ ).<sup>45</sup> An electrocatalyst possessing a lowered electrocatalytic barrier should have a smaller  $\Delta E$  value.<sup>46</sup> In the case of Ag/NCO-HS, the  $\Delta E$  was measured to be 0.93 V (Figure 5d), which is generally smaller than the reported carbon-free bifunctional electrocatalysts (see Table S3). After the Fe-doping treatment, the bifunctional  $\Delta E$  of Ag/FNCO-HS decreases further by 40 mV to Ag/NCO-HS (Figure 5d). Hence, we used the most active Ag/FNCO-HS as the main electrocatalyst for the bifunctional device studies.

**2.5. Operando Raman Spectroscopy.** To understand the phase transformation (i.e., phase, valences) at varied potentials of OER in the rock salt oxides, we conducted the operando Raman study. Under the dry conditions, Ag/NCO-HS (Figure 6a, green curve) exhibits a broad band at 550 cm<sup>-1</sup> that corresponds to the Co<sup>II</sup>–O vibrations (the blue highlight)<sup>47,48</sup> and a weak band at 670 cm<sup>-1</sup> associated with the octahedral-coordinated Co<sup>II</sup>–O stretch (the yellow highlight).<sup>48,49</sup> NiO has only one band at 550 cm<sup>-1</sup> corresponding to Ni<sup>II</sup>–O bonds, overlapping with that of Co<sup>II</sup>–O vibrations.<sup>50,51</sup> For Ag/FNCO-HS (Figure 6a, red curve), the band at 670 cm<sup>-1</sup> intensifies more than Ag/NCO-

Scheme 2. Illustrated Phase Transition of Rock Salt Ternary Oxides during the OER Process<sup>a</sup>

<sup>a</sup>The plane of the metal cation array is labeled by the pink dashed lines along the three phases, showing that no position change or interlayer migration of the corresponding metal cations occurs upon phase transformation. The octahedrally coordinated environments of metals are highlighted in blue, which remains nearly identical in each stage of phase transformation, supporting the highly reversible local environment from rock salt oxide to oxyhydroxide in OER.

HS due to the octahedral  $\text{Fe}^{\text{II}}\text{--O}$  vibrations falling on the same position as the octahedral-coordinated  $\text{Co}^{\text{II}}\text{--O}$  stretch.<sup>48,49</sup>

Immersing Ag/NCO-HS into 0.1 M KOH (Figure 6a, blue curve) results in a depletion of the  $\text{Co}^{\text{II}}\text{--O}$  stretch at  $670 \text{ cm}^{-1}$ , presumably due to the conversion of rock salt oxide into a hydroxide structure, although a supposedly  $\text{Co}^{\text{II}}\text{--OH}$  vibration of  $\text{Co}(\text{OH})_2$  at  $450 \text{ cm}^{-1}$  (pink highlight) remains insignificantly present.<sup>48,52</sup> The common peak of  $\text{NiO}/\text{CoO}$  exhibits a slight blue shift from  $550$  to  $560 \text{ cm}^{-1}$ , also corresponding to this structural transformation.<sup>53</sup> On the other hand, immersion of Ag/FNCO-HS in 0.1 M KOH (Figure 6a, black curve) causes the intense peak at  $670 \text{ cm}^{-1}$  to nearly flatten with an appreciable rise of the  $\text{M}^{\text{II}}\text{--OH}$  at  $450 \text{ cm}^{-1}$  ( $\text{M} = \text{Co}$  and  $\text{Fe}$ , the pink highlight).<sup>54</sup> These results further confirm the transformation of rock salt oxide into hydroxide, which is significantly enhanced in the presence of the  $\text{Fe}^{\text{II}}$  dopant. In addition,  $\text{Fe}^{\text{II}}\text{--OH}$  has a signal at  $550 \text{ cm}^{-1}$  that supplements the  $\text{Ni}^{\text{II}}\text{--O}/\text{Co}^{\text{II}}\text{--O}$  signals, leading to the inappreciable peak shift on the  $550 \text{ cm}^{-1}$  band, as compared to Ag/NCO-HS.<sup>54</sup>

The potential-dependent phase transformation under OER charging from the rest (at  $0.865 \text{ V}$ ) to OER conditions (at  $2.265 \text{ V}$ ) is shown in Figure 6d,e, where the fully charged active species are both indexed as MOOH ( $\text{M} = \text{Co}^{3+}$  and  $\text{Ni}^{3+}$ ). At the charged state, the strong band at  $470 \text{ cm}^{-1}$ , together with the relatively weak one at  $550 \text{ cm}^{-1}$ , corresponds to the presence of  $\text{NiOOH}$ .<sup>55–58</sup> Meanwhile, the shoulder at around  $600 \text{ cm}^{-1}$  (black arrow in Figure 6d), corresponding to  $\text{Co}^{\text{III}}\text{--O}$  vibrations in  $\text{CoOOH}$ ,<sup>56,59</sup> appears to coincide with the  $\text{NiOOH}$  peaks. Another peak also corresponding to  $\text{CoOOH}$  at  $\sim 500 \text{ cm}^{-1}$  is unobservable due to the overshadowing of  $\text{NiOOH}$  signals. The oxidation of  $\text{Co}^{\text{III}}\text{OOH}$  to  $\text{Co}^{\text{IV}}\text{O}_2$  at the elevated potentials is difficult to identify exclusively, due to a small peak shift and the strong overshadowing signals from  $\text{NiOOH}$ .<sup>59</sup> As Co and Ni evenly occupies all of the octahedral sites (i.e.,  $\text{Ni}/\text{Co} \approx 1$ ), their phase transformation should be strongly influenced by the common structure effect of oxyhydroxide.

In comparison, the operando Raman curves of Ag/FNCO-HS (Figure 6e) are similar to those of Ag/NCO-HS under the fully charged conditions, except the slight band broadening due to the structural incorporation of an  $\text{FeO}$  impurity.<sup>60</sup> The Raman data also show earlier activation at  $1.265 \text{ V}$  (Figure 6e, green) than the iron-free electrocatalysts at  $1.365 \text{ V}$  (Figure 6d, cyan), where the signal at  $470 \text{ cm}^{-1}$  starts to arise. In addition, the iron oxyhydroxide signal at  $675 \text{ cm}^{-1}$  is absent at  $1.865 \text{ V}$  (Figure 6e, black). These results collectively suggest that the iron dopants promote  $\text{NiOOH}/\text{CoOOH}$  activation, rather than forming  $\text{FeOOH}$  to participate in OER electrocatalysis as reported by Niu et al.<sup>61</sup> The corresponding LSV (Figure 5c) reveals the higher population of  $\text{Ni}^{2+/3+}$  activation in the presence of iron, further supporting the role of iron in lowering the structural transformation barrier. A small amount of  $\text{Fe}^{2+}$  doping could stabilize the high-valent state of Ni sites and thus decrease the activation potentials.<sup>44</sup> As such, the extensive  $\text{Ni}^{2+/3+}$  conversion suggests that  $\text{NiOOH}$  is the major active site for OER, while  $\text{CoOOH}$  and/or  $\text{Co}_2$  act as the cocatalyst.

The long-term stability of electrocatalysts depends on the reversibility of phase transformation in a cyclic charge/discharge operation. We thus monitored Ag/FNCO-HS from the rest condition (Figure 6b, black curve) to the fully charged status at  $2.365 \text{ V}$  (Figure 6b, green) and then discharged the electrocatalysts immediately back to the rest conditions (Figure 6b, red) as a complete charge/discharge cycle. After repeating this process several times (Figure 6c), the discharged state shows the three characteristic bands at  $450$  (red band),  $550$  (blue band), and  $670 \text{ cm}^{-1}$  (orange band) similar to the fresh electrocatalysts before any tests, indicative of high structural reversibility in OER. This reversible transformation suggests that the octahedral coordination units ( $\text{M} = \text{Co}$ ,  $\text{Fe}$ , and  $\text{Ni}$ ) of the rock salt structure are not significantly altered during the charging/discharging process.

The rock salt structure is entirely comprised of octahedral ( $\text{MO}_6$ ) units, which should minimize the transformation barrier, in contrast to mixed local environments. Mixed

coordination of octahedral ( $\text{MO}_6$ ) and tetrahedral ( $\text{MO}_4$ ) sites in spinel oxides (also recognized as a widely reported OER-active phase in the literature, such as  $\text{Co}_3\text{O}_4$ ) could increase the barrier of structural reversibility and the probability of deconstructive transformation after the cyclic OER operation. The difference between crystal field stabilization energies (CFSE) of low-spin  $\text{Co}_{\text{O}_h}^{2+}$  ( $t_{2g}^6 e_g^1$ ) to  $\text{Co}_{\text{O}_h}^{3+}$  ( $t_{2g}^6 e_g^0$ ) is only  $3/5\Delta_{\text{O}_h}$  (without counting pairing energy), much lower than the energy required to oxidize  $\text{Co}_{\text{T}_d}^{2+}$  to  $\text{Co}_{\text{T}_d}^{3+}$ . Likewise, metal oxidation in a  $\text{T}_d$  environment of spinel oxides can be less energy favorable than a sole  $\text{O}_h$  environment.<sup>49</sup> Intersystem coordination rearrangement between  $\text{O}_h$  and  $\text{T}_d$  systems can be even more energy unfavorable.

The reversible structural transformation of the rock salt oxides, according to the above data, is illustrated in Scheme 2. The dashed line aligns the metal cation layer among phases of rock salt, metal hydroxides, and metal oxyhydroxides. One can find that migration of metal cations to other positions or layers is not required upon phase transformation, as all of the metal cations sit only in a six oxygen-coordinated environment (no  $\text{T}_d$  sites). The structure alteration only occurs at the changes of interlayer *d*-spacing due to electrolyte interactions. These characteristics give rise to a reliable structural reversibility during the rapid cyclic OER tests with Ag/FNCO-HS. These unique rock salt-enabled characteristics are essential criteria for the durable performance of bifunctional cells.

**2.6. Device Performance.** The bifunctional performance was evaluated in an anion-exchange membrane (AEM) device under electrolyzer (OER) and fuel cell modes (ORR), as shown in Figure 7a. Ag/FNCO-HS requires a lower potential (2.03 V) than the benchmark  $\text{RuO}_2$  (2.16 V) to reach a current density of  $1000 \text{ mA cm}^{-2}$  (Figure 7b), agreeing with the three-electrode measurement where Ag/FNCO-HS requires a lower OER overpotential ( $\eta = 282 \text{ mV}$ ) than  $\text{RuO}_2$  ( $\eta = 340 \text{ mV}$ ). As the bulk electrical conductivity of the electrocatalysts has a critical influence on device performance,<sup>62,63</sup> the measured bulk electrical conductivity of Ag/FNCO-HS ( $1.1 \times 10^{-1} \text{ S cm}^{-1}$ ) and  $\text{RuO}_2$  ( $2 \times 10^{-1} \text{ S cm}^{-1}$ ) possesses comparable values. The greater electrolyzer performance of Ag/FNCO-HS than  $\text{RuO}_2$  is most likely due to the intrinsic electrocatalytic activities, rather than the conductivity effect. On testing the stability with a relatively high current density ( $\sim 200 \text{ mA cm}^{-2}$ ) at 1.5 V for 3 h,<sup>62</sup> Ag/FNCO-HS shows higher durability (<0.1% decay) compared to  $\text{RuO}_2$  (5.5% decay) (Figure 7c). The EIS of the Ag/FNCO-HS device shows no obvious change after the stability test (inset of Figure 7c), while the charge-transfer and mass transport resistances of the  $\text{RuO}_2$  cell apparently increased. The current decrease of the  $\text{RuO}_2$  cell may be due to passivation/dissolution or any potential irreversible phase transformation of electrocatalysts.

The AEM fuel cell functionality was tested with the same cell assembly as above but changing the flow direction of  $\text{H}_2$  and  $\text{O}_2$ , as indicated in Figure 7a. We fabricated the reference devices utilizing benchmark Pt/C as the ORR electrocatalyst for comparison. As shown in Figure 7d, Ag/FNCO-HS shows a higher open-circuit voltage (OCV) of 0.90 V than Pt/C (0.81 V) and exhibits higher working potentials than the Pt/C device at various current densities (Figure 7d; curves of red squares and black dots). Ag/FNCO-HS indeed possesses a lower activation energy barrier than Pt/C.<sup>48,49</sup> At the targeted current output (i.e.,  $44 \text{ mA cm}^{-2}$  for platinum group-free fuel

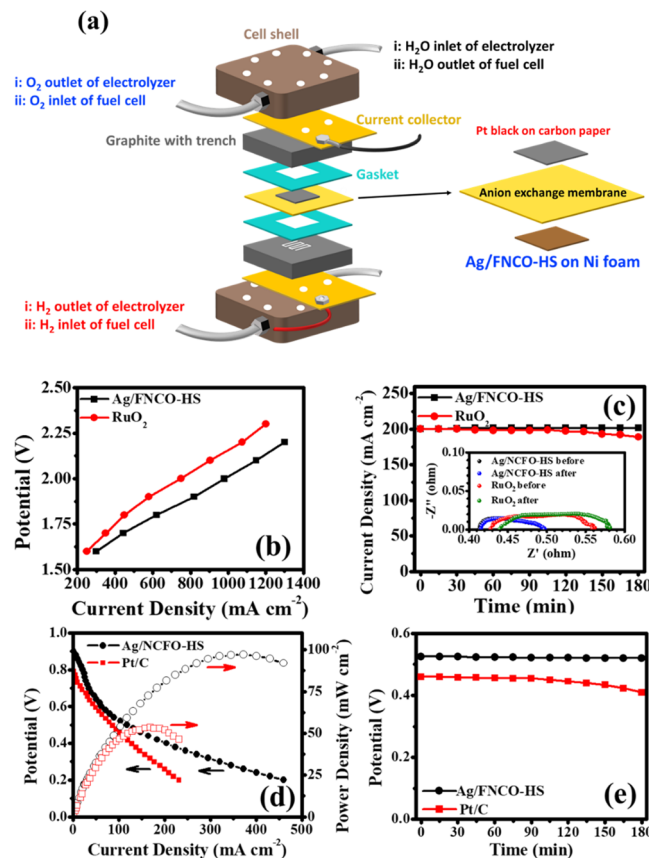


**Figure 7.** Bifunctional device performance using the Ag/NCO-HS catalyst as compared to the benchmarks. (a) Cell assembly of the AEM device where the inlets and outlets for electrolyzer and fuel cell modes are labeled (i) and (ii), respectively. (b) Electrolyzer mode performance comparison between Ag/NCO-HS and  $\text{RuO}_2$  as alkaline OER electrocatalysts. (c) Corresponding stability tests of catalysts in (b) at a constant potential of 1.50 V, where the inset shows the EIS of the corresponding devices measured before and after the stability tests. (d) Fuel cell mode performance comparison between Ag/NCO-HS and Pt as the alkaline ORR electrocatalysts. (e) Stability tests of the catalysts in (d) at a constant current density of  $100 \text{ mA cm}^{-2}$ .

cells),<sup>50</sup> Ag/NCO-HS shows a higher potential (0.66 V) than the Pt/C device (0.61 V). Moreover, the maximum power density of the Ag/NCO-HS device is  $96.98 \text{ mW cm}^{-2}$ , almost two times higher than that of the Pt/C devices (hollow red square and open-dot curves in Figure 6d), suggesting that Ag/NCO-HS allows better energy conversion than Pt/C.

Notably, the performance of Ag/NCO-HS is greater than Pt/C in the real device conditions but reverse in an ideal three-electrode system. The accessible exposure of a catalyst to electrolyte ions ( $\text{OH}^-$ ) in a real device is mainly governed by its junction interface with the AEM membrane. This factor cannot be incorporated into a three-electrode system, as the catalyst experiences full liquid electrolyte exposure. In Pt/C, the irreversible Pt-catalyzed corrosion of carbon hampers the ion transport due to the impaired junction interface, which significantly decays the ORR performance in a device despite its high performance in the three-electrode system.<sup>64,65</sup> As such, the carbon-free Ag/NCO-HS avoids the junction impairment between catalysts and AEM, leading to better ORR performance than Pt/C in the fuel cell mode. In the stability test of the fuel cell mode at a constant current density

of  $100 \text{ mA cm}^{-2}$ ,<sup>66</sup> the Ag/FNCO-HS cell shows a higher stability with only 0.1% decay, compared to the Pt/C fuel cell (10.9% decay) after a 3 h test (Figure 7e). The relatively large decay in Pt/C may arise from the typical electrochemical corrosion of the carbon component.<sup>9</sup>

To evaluate the interchangeable performance, the device was first conducted in the electrolyzer mode with Ag/FNCO-HS on the oxygen evolution electrode, followed by switching to the fuel cell mode with  $\text{O}_2$  going through the Ag/FNCO-HS electrodes. Switching from electrolyzer to fuel cell modes is considered as one complete cycle. After a 10-cycle test, the Ag/FNCO-HS electrodes show nearly identical bifunctional performance (Figure 8a), while the Pt/C-based oxygen

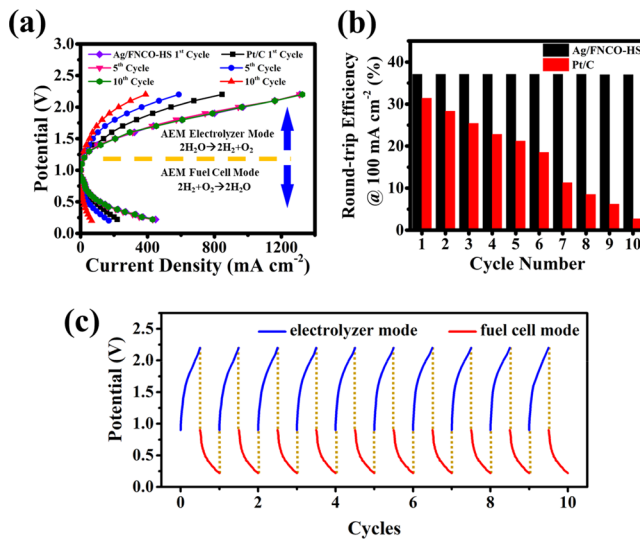


**Figure 8.** Comparison of the performance of AEM devices between electrolyzer and fuel cell modes using Ag/FNCO-HS and Pt/C. (a) Polarization curves of the devices measured over 10 cycles, where each cycle includes one electrolyzer test, followed by one run of the fuel cell mode. (b) Round-trip efficiency (based on eq 1) at  $100 \text{ mA cm}^{-2}$  for 10 cycles. The carbon-free Ag/FNCO-HS shows higher durability than carbon-based Pt/C. (c) Data set of the cycle tests, where the yellow dotted lines indicate the swapping in each cycle. The maximum current densities achieved are  $1.3 \text{ A cm}^{-2}$  and  $430 \text{ mA cm}^{-2}$  for the electrolyzer and fuel cell modes, respectively.

evolution electrode in a reference device reveals a significant electrolyzer decay by losing 61.1% of current density (at 1.5 V) and fuel cell decay by losing 80.6% of current density (at 0.5 V). To quantify the bifunctional efficiency, the ratios between the potentials obtained in both fuel cell and electrolyzer modes are calculated as round-trip efficiency, which is described by the following equation<sup>3</sup>

$$\text{round - trip efficiency} = \frac{V_{\text{fuel cell}}}{V_{\text{electrolyzer}}} \times 100\% \quad (1)$$

where  $V_{\text{fuel cell}}$  is the potential generated at  $100 \text{ mA cm}^{-2}$  in the fuel cell mode and  $V_{\text{electrolyzer}}$  is the potential required to reach  $100 \text{ mA cm}^{-2}$  in the electrolyzer mode.

The  $V_{\text{electrolyzer}}$  of Ag/FNCO-HS devices required 1.40 V in water splitting and generated electricity of 0.52 V as a fuel cell. Thus, the devices show a round-trip efficiency of 37.1% in the first cycle and retain the same after the 10th cycle (Figure 8b).<sup>3</sup> In contrast, carbon-based Pt/C shows a round-trip efficiency of 31.4% in the first cycle but gradually decreases to 2.4% in the

10th cycle due to carbon corrosion.<sup>3</sup> The carbon-free nature of Ag/FNCO-HS avoids decay in carbon components under anodic OER conditions,<sup>67,68</sup> resulting in high robustness under electrolyzer-fuel cell cycling (Figure 8c). The structural reversibility also aids the long-term durability of device applications.

### 3. CONCLUSIONS

We successfully prepared highly dispersible, carbon-free electrocatalysts based on ternary rock salt oxides exhibiting durable performance in bifunctional AEM devices. The exceptional device performance of Ag/FNCO-HS as compared to benchmarks of Pt/C and RuO<sub>2</sub> has been accomplished. The carbon-free nature eliminates the corrosion issue, the hollow structure preserves suspension ability, and the homogeneous rock salt oxides create a new route of achieving structural reversibility and durability even under the harsh conditions of cyclic tests. Our Raman study confirms the key characteristic of the highly reversible structure and iron-promoted phase transformation responsible for the exceptional bifunctional performance. Further adjustment of elemental ratios in multinary rock salt oxides is therefore anticipated to optimize the device performance in future studies. Rapid and simplified syntheses of metal/metal oxide hollow spheres are also needed to truly achieve massive-scale applications.

### ASSOCIATED CONTENT

#### Supporting Information

The Supporting Information is available free of charge at <https://pubs.acs.org/doi/10.1021/acsaem.0c03209>.

Experimental procedures; synthetic procedure scheme; embedded Ag particle size histogram; characterization data (EDS, XPS); OER stability tests; electrochemical surface area; ORR electrochemical data (electron-transfer number, hydrogen peroxide yield, electrochemical impedance, and methanol crossover); iron doping comparisons (XRD, ORR LSV, and ICP-MS data); and comparison tables (versus benchmarks and other catalysts in the literature) ([PDF](#))

### AUTHOR INFORMATION

#### Corresponding Author

Chun-Hu Chen – Department of Chemistry, National Sun Yat-sen University, Kaohsiung 80424, Taiwan; [orcid.org/0000-0002-3512-6880](#); Email: [chunhu.chen@mail.nsysu.edu.tw](mailto:chunhu.chen@mail.nsysu.edu.tw)

#### Authors

Po-Chun Liao – Department of Chemistry, National Sun Yat-sen University, Kaohsiung 80424, Taiwan

Ren-Huai Jhang – Department of Chemistry, National Sun Yat-sen University, Kaohsiung 80424, Taiwan; [orcid.org/0000-0002-8439-5446](#)

Yu-Hsiang Chiu – Department of Chemistry, National Sun Yat-sen University, Kaohsiung 80424, Taiwan

Joey Andrew A. Valinton – Department of Chemistry, National Sun Yat-sen University, Kaohsiung 80424, Taiwan; [orcid.org/0000-0002-5244-3765](#)

Chia-Hao Yeh – Department of Chemistry, National Sun Yat-sen University, Kaohsiung 80424, Taiwan

Virgilio D. Ebajo, Jr. – Department of Chemistry, National Sun Yat-sen University, Kaohsiung 80424, Taiwan;

Chemistry Department, College of Science, De La Salle University, Manila 1004, Philippines

Ching-Hsuan Wang – Department of Chemistry, National Sun Yat-sen University, Kaohsiung 80424, Taiwan

Complete contact information is available at:  
<https://pubs.acs.org/10.1021/acsaem.0c03209>

## Author Contributions

This manuscript was written through contributions of all authors. All authors have given approval to the final version of the manuscript.

## Notes

The authors declare no competing financial interest.

## ACKNOWLEDGMENTS

We acknowledge financial support from the Ministry of Science and Technology, Taiwan, under grant 108-2113-M-110-002, and the New Southbound Project of Academic Alliance supported by the Ministry of Education, Taiwan. We also thank Prof. Steven Suib for help with electron microscopy.

## REFERENCES

- (1) Wagner, F. T.; Lakshmanan, B.; Mathias, M. F. Electrochemistry and the Future of the Automobile. *J. Phys. Chem. Lett.* **2010**, *1*, 2204–2219.
- (2) Yang, Z.; Zhang, J.; Kintner-Meyer, M. C. W.; Lu, X.; Choi, D.; Lemmon, J. P.; Liu, J. Electrochemical Energy Storage for Green Grid. *Chem. Rev.* **2011**, *111*, 3577–3613.
- (3) Ng, J. W. D.; Tang, M.; Jaramillo, T. F. A carbon-free, precious-metal-free, high-performance O<sub>2</sub> electrode for regenerative fuel cells and metal-air batteries. *Energy Environ. Sci.* **2014**, *7*, 2017–2024.
- (4) Park, S.; Shao, Y.; Liu, J.; Wang, Y. Oxygen electrocatalysts for water electrolyzers and reversible fuel cells: status and perspective. *Energy Environ. Sci.* **2012**, *5*, 9331–9344.
- (5) Desmond Ng, J. W.; Gorlin, Y.; Hatsukade, T.; Jaramillo, T. F. A Precious-Metal-Free Regenerative Fuel Cell for Storing Renewable Electricity. *Adv. Energy Mater.* **2013**, *3*, 1545–1550.
- (6) Gupta, S.; Zhao, S.; Wang, X. X.; Hwang, S.; Karakalos, S.; Devaguptapu, S. V.; Mukherjee, S.; Su, D.; Xu, H.; Wu, G. Quaternary FeCoNiMn-Based Nanocarbon Electrocatalysts for Bifunctional Oxygen Reduction and Evolution: Promotional Role of Mn Doping in Stabilizing Carbon. *ACS Catal.* **2017**, *7*, 8386–8393.
- (7) Wu, Z.-S.; Yang, S.; Sun, Y.; Parvez, K.; Feng, X.; Müllen, K. 3D Nitrogen-Doped Graphene Aerogel-Supported Fe<sub>3</sub>O<sub>4</sub> Nanoparticles as Efficient Electrocatalysts for the Oxygen Reduction Reaction. *J. Am. Chem. Soc.* **2012**, *134*, 9082–9085.
- (8) Kao, W.-Y.; Chen, W.-Q.; Chiu, Y.-H.; Ho, Y.-H.; Chen, C.-H. General Solvent-dependent Strategy toward Enhanced Oxygen Reduction Reaction in Graphene/Metal Oxide Nanohybrids: Effects of Nitrogen-containing Solvent. *Sci. Rep.* **2016**, *6*, No. 37174.
- (9) Jang, S.-E.; Kim, H. Effect of Water Electrolysis Catalysts on Carbon Corrosion in Polymer Electrolyte Membrane Fuel Cells. *J. Am. Chem. Soc.* **2010**, *132*, 14700–14701.
- (10) Lan, W.-J.; Kuo, C.-C.; Chen, C.-H. Hierarchical nanostructures with unique Y-shaped interconnection networks in manganese substituted cobalt oxides: the enhancement effect on electrochemical sensing performance. *Chem. Commun.* **2013**, *49*, 3025–3027.
- (11) Kuo, C.-C.; Lan, W.-J.; Chen, C.-H. Redox preparation of mixed-valence cobalt manganese oxide nanostructured materials: highly efficient noble metal-free electrocatalysts for sensing hydrogen peroxide. *Nanoscale* **2014**, *6*, 334–341.
- (12) Deng, X.; Öztürk, S.; Weidenthaler, C.; Tüysüz, H. Iron-Induced Activation of Ordered Mesoporous Nickel Cobalt Oxide Electrocatalyst for the Oxygen Evolution Reaction. *ACS Appl. Mater. Interfaces* **2017**, *9*, 21225–21233.
- (13) Kuboon, S.; Hu, Y. H. Study of NiO–CoO and Co<sub>3</sub>O<sub>4</sub>–Ni<sub>3</sub>O<sub>4</sub> Solid Solutions in Multiphase Ni–Co–O Systems. *Ind. Eng. Chem. Res.* **2011**, *50*, 2015–2020.
- (14) Trotochaud, L.; Ranne, J. K.; Williams, K. N.; Boettcher, S. W. Solution-Cast Metal Oxide Thin Film Electrocatalysts for Oxygen Evolution. *J. Am. Chem. Soc.* **2012**, *134*, 17253–17261.
- (15) Sakata, T.; Sakata, K. Change of Oxygen Concentration with Temperature of the Nickel and Cobalt Oxide Solid Solution. *J. Phys. Soc. Jpn.* **1958**, *13*, 675–683.
- (16) Chen, W.-Q.; Chung, M.-C.; Valinton, J. A. A.; Penalosa, D. P.; Chuang, S.-H.; Chen, C.-H. Heterojunctions of silver–iron oxide on graphene for laser-coupled oxygen reduction reactions. *Chem. Commun.* **2018**, *54*, 7900–7903.
- (17) Nørskov, J. K.; Rossmeisl, J.; Logadottir, A.; Lindqvist, L.; Kitchin, J. R.; Bligaard, T.; Jónsson, H. Origin of the Overpotential for Oxygen Reduction at a Fuel-Cell Cathode. *J. Phys. Chem. B* **2004**, *108*, 17886–17892.
- (18) Mohammadkhani, S.; Schaal, E.; Dolatabadi, A.; Moreau, C.; Davis, B.; Guay, D.; Roué, L. Synthesis and thermal stability of (Co,Ni)O solid solutions. *J. Am. Ceram. Soc.* **2019**, *102*, 5063–5070.
- (19) Liyanage, D. R.; Danforth, S. J.; Liu, Y.; Bussell, M. E.; Brock, S. L. Simultaneous Control of Composition, Size, and Morphology in Discrete Ni<sub>2</sub>–xCo<sub>x</sub>P Nanoparticles. *Chem. Mater.* **2015**, *27*, 4349–4357.
- (20) Crystal Ionic Radii of the Elements. In *CRC Handbook of Chemistry and Physics*, 1st ed.; Weast, R. C., Ed.; CRC Press, 1987; p F-105.
- (21) Grosvenor, A. P.; Biesinger, M. C.; Smart, R. S. C.; McIntyre, N. S. New interpretations of XPS spectra of nickel metal and oxides. *Surf. Sci.* **2006**, *600*, 1771–1779.
- (22) Thi, T. V.; Rai, A. K.; Gim, J.; Kim, J. High performance of Co-doped NiO nanoparticle anode material for rechargeable lithium ion batteries. *J. Power Sources* **2015**, *292*, 23–30.
- (23) Zheng, Y.; Zheng, L.; Zhan, Y.; Lin, X.; Zheng, Q.; Wei, K. Ag/ZnO Heterostructure Nanocrystals: Synthesis, Characterization, and Photocatalysis. *Inorg. Chem.* **2007**, *46*, 6980–6986.
- (24) Walton, A. S.; Fester, J.; Bajdich, M.; Arman, M. A.; Osiecki, J.; Knudsen, J.; Vojvodic, A.; Lauritsen, J. V. Interface Controlled Oxidation States in Layered Cobalt Oxide Nanoislands on Gold. *ACS Nano* **2015**, *9*, 2445–2453.
- (25) Hou, Y.; Liu, Y.; Gao, R.; Li, Q.; Guo, H.; Goswami, A.; Zboril, R.; Gawande, M. B.; Zou, X. Ag@Co<sub>x</sub>P Core–Shell Heterogeneous Nanoparticles as Efficient Oxygen Evolution Reaction Catalysts. *ACS Catal.* **2017**, *7*, 7038–7042.
- (26) Zhang, Z.; Li, X.; Zhong, C.; Zhao, N.; Deng, Y.; Han, X.; Hu, W. Spontaneous Synthesis of Silver-Nanoparticle-Decorated Transition-Metal Hydroxides for Enhanced Oxygen Evolution Reaction. *Angew. Chem., Int. Ed.* **2020**, *59*, 7245–7250.
- (27) Lu, J.; Zhou, W.; Wang, L.; Jia, J.; Ke, Y.; Yang, L.; Zhou, K.; Liu, X.; Tang, Z.; Li, L.; Chen, S. Core–Shell Nanocomposites Based on Gold Nanoparticle@Zinc–Iron-Embedded Porous Carbons Derived from Metal–Organic Frameworks as Efficient Dual Catalysts for Oxygen Reduction and Hydrogen Evolution Reactions. *ACS Catal.* **2016**, *6*, 1045–1053.
- (28) He, H.; Chen, J.; Zhang, D.; Li, F.; Chen, X.; Chen, Y.; Bian, L.; Wang, Q.; Duan, P.; Wen, Z.; Lv, X. Modulating the Electrocatalytic Performance of Palladium with the Electronic Metal–Support Interaction: A Case Study on Oxygen Evolution Reaction. *ACS Catal.* **2018**, *8*, 6617–6626.
- (29) Chala, S. A.; Tsai, M.-C.; Su, W.-N.; Ibrahim, K. B.; Thirumalraj, B.; Chan, T.-S.; Lee, J.-F.; Dai, H.; Hwang, B.-J. Hierarchical 3D Architectured Ag Nanowires Shelled with NiMn-Layered Double Hydroxide as an Efficient Bifunctional Oxygen Electrocatalyst. *ACS Nano* **2020**, *14*, 1770–1782.
- (30) Chala, S. A.; Tsai, M.-C.; Su, W.-N.; Ibrahim, K. B.; Duma, A. D.; Yeh, M.-H.; Wen, C.-Y.; Yu, C.-H.; Chan, T.-S.; Dai, H.; Hwang, B.-J. Site Activity and Population Engineering of NiRu-Layered Double Hydroxide Nanosheets Decorated with Silver Nanoparticles

- for Oxygen Evolution and Reduction Reactions. *ACS Catal.* **2019**, *9*, 117–129.
- (31) Mandal Goswami, M. Synthesis of Micelles Guided Magnetite ( $\text{Fe}_3\text{O}_4$ ) Hollow Spheres and their application for AC Magnetic Field Responsive Drug Release. *Sci. Rep.* **2016**, *6*, No. 35721.
- (32) Xu, Y.; Bian, W.; Wu, J.; Tian, J.-H.; Yang, R. Preparation and electrocatalytic activity of 3D hierarchical porous spinel  $\text{CoFe}_2\text{O}_4$  hollow nanospheres as efficient catalyst for Oxygen Reduction Reaction and Oxygen Evolution Reaction. *Electrochim. Acta* **2015**, *151*, 276–283.
- (33) Zeng, L.; Sun, K.; Chen, Y.; Liu, Z.; Chen, Y.; Pan, Y.; Zhao, R.; Liu, Y.; Liu, C. Neutral-pH overall water splitting catalyzed efficiently by a hollow and porous structured ternary nickel sulfoselenide electrocatalyst. *J. Mater. Chem. A* **2019**, *7*, 16793–16802.
- (34) Moysiadou, A.; Hu, X. Stability profiles of transition metal oxides in the oxygen evolution reaction in alkaline medium. *J. Mater. Chem. A* **2019**, *7*, 25865–25877.
- (35) Burke, M. S.; Kast, M. G.; Trotochaud, L.; Smith, A. M.; Boettcher, S. W. Cobalt–Iron (Oxy)hydroxide Oxygen Evolution Electrocatalysts: The Role of Structure and Composition on Activity, Stability, and Mechanism. *J. Am. Chem. Soc.* **2015**, *137*, 3638–3648.
- (36) Vishnu Prataap, R. K.; Mohan, S. Electrodeposited-hydroxide surface-covered porous nickel–cobalt alloy electrodes for efficient oxygen evolution reaction. *Chem. Commun.* **2017**, *53*, 3365–3368.
- (37) Smith, R. D. L.; Prévot, M. S.; Fagan, R. D.; Trudel, S.; Berlinguet, C. P. Water Oxidation Catalysis: Electrocatalytic Response to Metal Stoichiometry in Amorphous Metal Oxide Films Containing Iron, Cobalt, and Nickel. *J. Am. Chem. Soc.* **2013**, *135*, 11580–11586.
- (38) Lv, X.; Zhu, Y.; Jiang, H.; Yang, X.; Liu, Y.; Su, Y.; Huang, J.; Yao, Y.; Li, C. Hollow mesoporous  $\text{NiCo}_2\text{O}_4$  nanocages as efficient electrocatalysts for oxygen evolution reaction. *Dalton Trans.* **2015**, *44*, 4148–4154.
- (39) Tan, Y.; Xu, C.; Chen, G.; Fang, X.; Zheng, N.; Xie, Q. Facile Synthesis of Manganese-Oxide-Containing Mesoporous Nitrogen-Doped Carbon for Efficient Oxygen Reduction. *Adv. Funct. Mater.* **2012**, *22*, 4584–4591.
- (40) Men, B.; Sun, Y.; Tang, Y.; Zhang, L.; Chen, Y.; Wan, P.; Pan, J. Highly Dispersed Ag-Functionalized Graphene Electrocatalyst for Oxygen Reduction Reaction in Energy-Saving Electrolysis of Sodium Carbonate. *Ind. Eng. Chem. Res.* **2015**, *54*, 7415–7422.
- (41) Tamaki, T.; Yamauchi, A.; Ito, T.; Ohashi, H.; Yamaguchi, T. The Effect of Methanol Crossover on the Cathode Overpotential of DMFCs. *Fuel Cells* **2011**, *11*, 394–403.
- (42) Gong, L.; Chng, X. Y. E.; Du, Y.; Xi, S.; Yeo, B. S. Enhanced Catalysis of the Electrochemical Oxygen Evolution Reaction by Iron(III) Ions Adsorbed on Amorphous Cobalt Oxide. *ACS Catal.* **2018**, *8*, 807–814.
- (43) Stevens, M. B.; Trang, C. D. M.; Enman, L. J.; Deng, J.; Boettcher, S. W. Reactive Fe-Sites in Ni/Fe (Oxy)hydroxide Are Responsible for Exceptional Oxygen Electrocatalysis Activity. *J. Am. Chem. Soc.* **2017**, *139*, 11361–11364.
- (44) Cai, Z.; Zhou, D.; Wang, M.; Bak, S.-M.; Wu, Y.; Wu, Z.; Tian, Y.; Xiong, X.; Li, Y.; Liu, W.; Siahrostami, S.; Kuang, Y.; Yang, X.-Q.; Duan, H.; Feng, Z.; Wang, H.; Sun, X. Introducing  $\text{Fe}^{2+}$  into Nickel–Iron Layered Double Hydroxide: Local Structure Modulated Water Oxidation Activity. *Angew. Chem., Int. Ed.* **2018**, *57*, 9392–9396.
- (45) Ahmed, M. S.; Choi, B.; Kim, Y.-B. Development of Highly Active Bifunctional Electrocatalyst Using  $\text{Co}_3\text{O}_4$  on Carbon Nanotubes for Oxygen Reduction and Oxygen Evolution. *Sci. Rep.* **2018**, *8*, No. 2543.
- (46) Li, S.; Cheng, C.; Zhao, X.; Schmidt, J.; Thomas, A. Active Salt/Silica-Templated 2D Mesoporous  $\text{FeCo-N}_x$ -Carbon as Bifunctional Oxygen Electrodes for Zinc–Air Batteries. *Angew. Chem., Int. Ed.* **2018**, *57*, 1856–1862.
- (47) Rivas-Murias, B.; Salgueirño, V. Thermodynamic  $\text{CoO}-\text{Co}_3\text{O}_4$  crossover using Raman spectroscopy in magnetic octahedron-shaped nanocrystals. *J. Raman Spectrosc.* **2017**, *48*, 837–841.
- (48) Yang, J.; Liu, H.; Martens, W. N.; Frost, R. L. Synthesis and Characterization of Cobalt Hydroxide, Cobalt Oxyhydroxide, and Cobalt Oxide Nanodiscs. *J. Phys. Chem. C* **2010**, *114*, 111–119.
- (49) Wang, X.; Liu, Y.; Zhang, T.; Luo, Y.; Lan, Z.; Zhang, K.; Zuo, J.; Jiang, L.; Wang, R. Geometrical-Site-Dependent Catalytic Activity of Ordered Mesoporous Co-Based Spinel for Benzene Oxidation: In Situ DRIFTS Study Coupled with Raman and XAFS Spectroscopy. *ACS Catal.* **2017**, *7*, 1626–1636.
- (50) Wu, Z.; Zou, Z.; Huang, J.; Gao, F. Fe-doped NiO mesoporous nanosheets array for highly efficient overall water splitting. *J. Catal.* **2018**, *358*, 243–252.
- (51) Rojas, E.; Delgado, J. J.; Guerrero-Pérez, M. O.; Bañares, M. A. Performance of NiO and Ni–Nb–O active phases during the ethane ammoxidation into acetonitrile. *Catal. Sci. Technol.* **2013**, *3*, 3173–3182.
- (52) Del Pilar-Albaladejo, J.; Dutta, P. K. Topotactic Transformation of Zeolite Supported Cobalt(II) Hydroxide to Oxide and Comparison of Photocatalytic Oxygen Evolution. *ACS Catal.* **2014**, *4*, 9–15.
- (53) Balram, A.; Zhang, H.; Santhanagopalan, S. Enhanced Oxygen Evolution Reaction Electrocatalysis via Electrodeposited Amorphous  $\alpha$ -Phase Nickel-Cobalt Hydroxide Nanodendrite Forests. *ACS Appl. Mater. Interfaces* **2017**, *9*, 28355–28365.
- (54) Thanos, I. C. G. In situ Raman and other studies of electrochemically oxidized iron and iron-9% chromium alloy. *Electrochim. Acta* **1986**, *31*, 811–820.
- (55) Lo, Y. L.; Hwang, B. J. In Situ Raman Studies on Cathodically Deposited Nickel Hydroxide Films and Electroless Ni–P Electrodes in 1 M KOH Solution. *Langmuir* **1998**, *14*, 944–950.
- (56) Zheng, W.; Liu, M.; Lee, L. Y. S. Electrochemical Instability of Metal–Organic Frameworks: In Situ Spectroelectrochemical Investigation of the Real Active Sites. *ACS Catal.* **2020**, *10*, 81–92.
- (57) Louie, M. W.; Bell, A. T. An Investigation of Thin-Film Ni–Fe Oxide Catalysts for the Electrochemical Evolution of Oxygen. *J. Am. Chem. Soc.* **2013**, *135*, 12329–12337.
- (58) Trześniewski, B. J.; Diaz-Morales, O.; Vermaas, D. A.; Longo, A.; Bras, W.; Koper, M. T. M.; Smith, W. A. In Situ Observation of Active Oxygen Species in Fe-Containing Ni-Based Oxygen Evolution Catalysts: The Effect of pH on Electrochemical Activity. *J. Am. Chem. Soc.* **2015**, *137*, 15112–15121.
- (59) Moysiadou, A.; Lee, S.; Hsu, C.-S.; Chen, H. M.; Hu, X. Mechanism of Oxygen Evolution Catalyzed by Cobalt Oxyhydroxide: Cobalt Superoxide Species as a Key Intermediate and Dioxygen Release as a Rate-Determining Step. *J. Am. Chem. Soc.* **2020**, *142*, 11901–11914.
- (60) Chen, C.-H.; Njagi, E. C.; Chen, S.-Y.; Horvath, D. T.; Xu, L.; Morey, A.; Mackin, C.; Joosten, R.; Suib, S. L. Structural Distortion of Molybdenum-Doped Manganese Oxide Octahedral Molecular Sieves for Enhanced Catalytic Performance. *Inorg. Chem.* **2015**, *54*, 10163–10171.
- (61) Niu, S.; Sun, Y.; Sun, G.; Rakov, D.; Li, Y.; Ma, Y.; Chu, J.; Xu, P. Stepwise Electrochemical Construction of  $\text{FeOOH}/\text{Ni(OH)}_2$  on Ni Foam for Enhanced Electrocatalytic Oxygen Evolution. *ACS Appl. Energy. Mater.* **2019**, *2*, 3927–3935.
- (62) Xu, D.; Stevens, M. B.; Cosby, M. R.; Oener, S. Z.; Smith, A. M.; Enman, L. J.; Ayers, K. E.; Capuano, C. B.; Renner, J. N.; Danilovic, N.; Li, Y.; Wang, H.; Zhang, Q.; Boettcher, S. W. Earth-Abundant Oxygen Electrocatalysts for Alkaline Anion-Exchange-Membrane Water Electrolysis: Effects of Catalyst Conductivity and Comparison with Performance in Three-Electrode Cells. *ACS Catal.* **2019**, *9*, 7–15.
- (63) Parrondo, J.; George, M.; Capuano, C.; Ayers, K. E.; Ramani, V. Pyrochlore electrocatalysts for efficient alkaline water electrolysis. *J. Mater. Chem. A* **2015**, *3*, 10819–10828.
- (64) Cifrain, M.; Kordes, K. V. Advances, aging mechanism and lifetime in AFCs with circulating electrolytes. *J. Power Sources* **2004**, *127*, 234–242.
- (65) Fujiwara, N.; Yao, M.; Siroma, Z.; Senoh, H.; Ioroi, T.; Yasuda, K. Reversible air electrodes integrated with an anion-exchange

membrane for secondary air batteries. *J. Power Sources* **2011**, *196*, 808–813.

(66) Liu, L.; Chu, X.; Liao, J.; Huang, Y.; Li, Y.; Ge, Z.; Hickner, M. A.; Li, N. Tuning the properties of poly(2,6-dimethyl-1,4-phenylene oxide) anion exchange membranes and their performance in H<sub>2</sub>/O<sub>2</sub> fuel cells. *Energy Environ. Sci.* **2018**, *11*, 435–446.

(67) Sapountzi, F. M.; Gracia, J. M.; Weststrate, C. J.; Fredriksson, H. O. A.; Niemantsverdriet, J. W. Electrocatalysts for the generation of hydrogen, oxygen and synthesis gas. *Prog. Energy Combust. Sci.* **2017**, *58*, 1–35.

(68) Huang, K. An Active and Robust Bifunctional Oxygen Electrocatalyst through Carbon-Free Hierarchical Functionalization. *Angew. Chem., Int. Ed.* **2017**, *56*, 12826–12827.